Shape-Driven Three-Dimensional Watersnake Segmentation of Biological Membranes in Electron Tomography

Hieu Nguyen and Qiang Ji*, *Senior Member, IEEE*

***Abstract*—Due to the significant complexity of membrane morphology and the generally poor image quality in electron tomographic volumes, current automatic methods for segmentation of membranes perform poorly. Users must resort to manual tracing of recognized patterns on 2-D slices of the volume, a method that suffers from subjectivity and is very labor intensive, preventing quantitative analyses of tomographic data that require comparative analyses of many volumes. To overcome these limitations, we develop an automatic 3-D segmentation method that fully exploits the prior knowledge about the shape of the membranes as well as the 3-D information provided by the tomograms, and systematically combines this knowledge with the image data to improve segmentation results. The method is based on the watersnake framework. By mathematically reformulating the traditional watershed segmentation as an energy minimization problem, the watersnake inherits the many strengths of the watershed method while overcoming the limitations of the traditional energy-based segmentation methods. In our previous work (H. Nguyen *et al.*, 2003), the original watersnake model was successfully modified by incorporating smoothness into watershed segmentation. In this work, we further extend that model to incorporate into the energy function various constraints representing our prior knowledge about the global shape of the cellular features to be segmented. Segmentation can, therefore, be accomplished via minimization of the energy function subject to the shape prior constraints. Finally, the mathematical framework is further extended from 2-D to 3-D so that segmentation can be carried out in 3-D to take advantage of the additional information provided by the tomograms. We apply this method for the automatic extraction of biological membranes of varying complexities including those of bacterial walls and mitochondrial boundaries.**

***Index Terms*—Electron tomography, image segmentation, membranes, watershed.**

I. Introduction and Significance

ELECTRON tomography is a method for determining 3-D structure by electron microscopy (EM), using multiple tilt views of the specimen [2], [3]. Electron tomograms contain, in principle, vast amounts of information on the locations and architectures of large numbers of subcellular assemblies and organelles at a resolution significantly higher than that which is possible with optical microscopy. In the relatively short time since its first applications in the late 1980s, electron tomography has provided numerous new insights into subcellular structure. A good example is the mitochondrion, whose textbook description has undergone major revision as a result of electron tomographic studies [4]–[7]. In the last five years, electron tomography has begun to evolve from a technique practiced in only a handful of specialized centers to one that is increasingly available to biomedical researchers.

A. Segmentation Bottleneck

However, even as the technology for producing tomographic reconstructions has become more sophisticated and accessible, and the data proliferate, the quantitative analysis and interpretation of the data remains a serious bottleneck. Quantitative analysis of electron tomograms typically involves segmenting cell components, measuring their dimensions, locating critical points, and determining spatial relations among the components (e.g., [6], [8], [9]). Segmentation is the identification and separation of components of interest from the complex and densely packed cellular environment characteristic of well-preserved biological specimens. Of all the steps involved in quantitative analysis of EM images, segmentation is particularly challenging, in part due to the tremendous complexity of biological features and in part due to poor EM image quality resulting from the low contrast of the input images (particularly when unstained, frozen-hydrated specimens are used), limited angular sampling, and an incomplete tilt range.

Because of these difficulties, segmenting cellular components has been dominated by manual procedures that rely on the expert knowledge of biologists to segment and recognize specific structures. For example, mitochondrial cristae can be segmented from electron-tomographic reconstructions by manual tracing. Such manual procedures, however, are time-consuming, subjective, prone to operator errors, and ill-suited to handling the data throughput required to make statistic correlations among datasets recorded under differing functional conditions. To mitigate these difficulties, several software packages have evolved specifically for the contouring of electron-tomographic data sets, including: SYNU [6], IMOD [10], [8], SPIDER/STERECON [11], [12], and NIH Image [13]. These software packages incorporate tools that provide a limited degree of operator assistance, e.g., placing spherical models in the location of vesicles as determined from a single contour; extending membranes drawn in one level to the next level in the volume, and "growing" linear objects such as microtubules from single lines [9], [10], [12], [14],

Manuscript received August 16, 2007; revised October 23, 2007. *Asterisk indicates corresponding author.*

H. Nguyen is with the Intelligent System Laboratory, Department of Electrical, Computer, and System Engineering, Rensselaer Polytechnic Institute, Troy, NY 12180 USA.

*Q. Ji is with the Intelligent System Laboratory Department of Electrical, Computer, and System Engineering, Rensselaer Polytechnic Institute, 110 8th Street, Troy, NY 12180 USA (e-mail: jig@rpi.edu).

Color versions of one or more of the figures in this paper are available online at http://ieeexplore.ieee.org.

Digital Object Identifier 10.1109/TMI.2007.912390

[15]. These computer approaches have been applied to segmentation projects in cellular electron tomography in several laboratories, e.g., Marsh *et al.*, 2001 [8], Harlow *et al.* 2001 [9], Segui-Simarro *et al.*, 2004 [16], Sosinsky *et al.*, 2005 [17]. However, the gain in project throughput provided by such tools is limited. For example, it took Marsh and colleagues [8] four months to produce a complex 3-D map of the Golgi region in part of a single pancreatic beta cell. This same group is now engaged in combining 50 or more tomographic reconstructions to map a large fraction of the cellular volume in order to understand patterns of vesicular trafficking [18]. The current level of sophistication of computer-assisted segmentation is woefully inadequate for this task. More importantly, the current approaches to computer-aided segmentation share several drawbacks with fully manual 2-D tracing of features. These include reliance on overly subjective criteria for feature extraction and delineation, and failure to utilize the full range of 3-D information in tomograms, which should provide important clues about feature shape and continuity.

B. Progress Toward Automated Segmentation

Over the years, automated segmentation techniques have also been developed for various EM applications. These methods can be grouped into two main categories: the energy minimization based approach and the watershed-based approach. Based on the minimization of an energy function, the energy-based approach can be further divided into the contour-based methods: the region-based method, and the graph-based method. The contour-based methods include active contours, active surface models (balloons), deformable models, and the level-set framework [19]. These methods have been successfully used in medical imaging for recognizing anatomical features from magnetic resonance imaging (MRI) images and scans [20]–[23]. Active contour applications to electron tomography include a geodesic active contour for segmentation of subcellular features in HIV-infected macrophages [24], parametric active contour to segment chromosomes from 3-D volumes [25], globally optimal geodesic active contours to cell microscopy [26], and active contour to achieve a 3-D reconstruction and segmentation of DNA filaments [27] using the level set method [28], [29]. In graph-based method, Frangakis and Hegrel [30] extended the normalized graph cut [31] for finding the boundaries between prokaryotic cells such as Pyrodictum abyssi and the ice in which they were embedded. Similarly, viruses were segmented successfully from the background and from the liposomes that served as mock host cells. The advantages of the traditional active contour-based methods include invariance to scale, size, and rotation. Despite the effort on improving the convergence of active contour [32], their common drawback is that they require high-contrast images, a good initial contour or surface model, and considerable fine-tuning of parameters in order to converge correctly. The recent work in active contour such as the one by Chan and Vese [33] has overcome some drawbacks with the traditional contour-based methods. Their method, however, is a region-based method relying on a unrealistic assumption of homogeneity of both foreground and background.

The watershed algorithm uses an immersion technique that is based upon analogy with the gradually flooding a topological relief by a fluid, with barriers built at the points where independent flows meet [34]–[37]. Volkmann [38] developed a 3-D version of the watershed algorithm for electron microscopy. This approach was effectively applied to a variety of electron-density maps, including in situ Golgi apparatus [39]. Their study demonstrates that the watershed method can segment membranes within the cellular context, and that the watershed method often produces excellent results for images with low complexity.

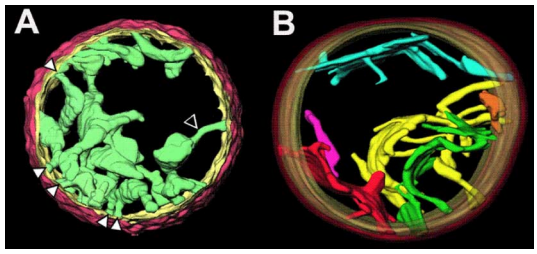

Fig. 1. Three-dimensional structure of mitochondrial membranes with outer membranes enclosing the inner membranes. (A). Surface rendering of the membranes in a condensed mitochondrion, prepared by conventional chemical fixation, plastic embedding, and heavy-metal staining. Arrows point to tubular crista junctions. (B). Surface rendering of the membranes in a mitochondrion suspended in 0.3 M sucrose, plunge-frozen at liquid nitrogen temperature, and imaged in a cryo-electron microscope.

While the automated segmentation methods achieved a certain degree of success in segmenting and tracing some cellular structures from EM images, these methods tend to be image data-driven only and therefore their success is limited to large and relatively simple structures. In addition, these methods can be fooled by subtle boundaries and image artifacts. We believe the performance of the automated segmentation techniques can be significantly improved by incorporating prior knowledge about the structure as well as the 3-D information into the segmentation process.

C. Significance of Biological Membranes

The planned focus on biological membranes stems from their central importance to biology. Biomembranes define most of the cell's internal compartments, acting both as barriers to diffusion and scaffolds for the molecular machinery associated with scores of processes, including energy transduction, protein trafficking, endo-and exocytosis, etc. In many cases, well-defined changes in local membrane topology are directly involved in these processes (endocytosis, viral budding); in other cases, transitions in overall membrane morphology ("remodeling") have been found to correlate with changes in functional state. A recent example is the dramatic remodeling of the mitochondrial inner membrane associated with mobilization of internal cytochrome prior to its release during apoptosis (see Fig. 1, topic reviewed in [40]).

The basic structure of most fungal, plant, and animal mitochondria under normal physiological conditions is the same: a smooth outer membrane that envelops an inner membrane whose surface area is considerably larger and which envelopes a protein-rich matrix. The inner membrane has numerous invaginations, cristae, each of which has one or more tubular connections to the membrane periphery. The crista morphology is generally not uniform and the junctions are not always short and circular [41], [4], [5]. A "typical" mitochondrial membrane morphology is shown in Fig. 1.

To give a sense of the scale of the problem, segmentation of large complex volumes typically can take days, weeks, or even months, as it did for Marsh *et al.* [8] to manually trace the membranes and cytoskeletal components in a serial tomographic reconstruction of part of one pancreatic cell. For individual liver mitochondria, manual tracing of the membranes in a single tomogram ($500 \times 500 \times 200$ voxels) typically requires 16–24 h. In the case of avian flight muscle mitochondria, which have a much greater density of cristae, it can take a week to trace a subvolume within the same size tomogram.

The goal of the proposed research is to develop a 3-D model-based approach for segmenting biological membranes of mitochondria and bacteria, fully exploiting any prior knowledge about the shapes of membranes. For the research reported in this paper, we introduce methods for automatically tracing the relatively simple inner and outer membrane boundaries in mitochondria and in bacteria such as E coli. Future work will extend current methods to segmenting the more complex cristae and their junctions. The main innovations of this research are: 1) mathematically combining the watershed segmentation and the prior shape information via the watersnakes model, 2) a novel application of the method to membrane segmentation based on systematic combination of the prior knowledge about the membranes with the image data, and 3) performing the watersnake segmentation in 3-D to take full advantage of the 3-D information that is currently lost when segmentation is performed on slices of tomograms. While 3-D watershed has been applied in other biological or medical imaging modalities [42], [43], its use in EM image has been limited, and in particular, the use of 3-D watershed with global shape prior is new.

While the focus of the proposed research is on segmentation of biological membranes in EM images, the proposed techniques will have wide applicability to other cellular structures in electron tomography and to other forms of medical imaging since the underlying theories of combining prior knowledge with image data remains true with other features. In addition, the proposed research may also be applicable to other modalities such as MRI and ultrasound since the quality of those modalities are at least as good, and usually better than EM images.

II. Literature Review on Model-Based Segmentation

The complexity of the biological features, the crowded environment, and the inherent low signal-to-noise ratio (SNR) present significant challenges to data-driven methods for segmentation in electron-tomographic reconstructions. On the other hand, the subcellular structures that we want to segment usually possess some distinctive geometric properties such as tubular structures of the cristad junctions at the membrane periphery and the very thin (5–10 nm) structure of membrane boundaries. This prior shape knowledge may be obtained from biologists, from statistical analysis of the training shapes, or acquired from user-drawn shapes, and they should be fully exploited to improve the segmentation accuracy and robustness.

While use of prior knowledge is relatively novel for segmentation of electron tomographic volumes, the concept has been widely adopted by segmentation in other modalities. We classify model-based segmentation techniques into three primary categories that differ in the way in which prior knowledge is incorporated into the segmentation procedure. The categories are: rigid modeling, constrained deformable modeling, and statistical shape modeling. One common rigid model-based method is template matching. In template matching [44], [45], the template is generally a structure that has been determined at high resolution, usually by an imaging modality other than electron microscopy (most often X-ray crystallography). After filtration of the template to match the approximate resolution of the electron-tomographic reconstruction, and direction-dependent adjustment to match the missing angular information, cross correlation is used to find objects matching the template in the 3-D tomographic reconstruction. Preliminary studies indicate that template matching is reasonably effective for identifying large macromolecular complexes such as chaperones in cell-free systems [44], [46] and ryanodine receptors in tomographic reconstructions of isolated triad junctions [47]. While encouraging, these preliminary efforts still struggle with false positives and have not yet been used to any appreciable extent to segment 3-D reconstructions of *in situ* cellular environment. Other major drawbacks of template matching include difficulty of constructing templates for complex biological structures and its inability to adapt to structure shape variability.

Constrained deformable modeling achieves improved robustness by using prior knowledge to constrain deformation. One way to achieve this is to incorporate size and shape constraints explicitly into the energy function of the active contour through a regularization term. This makes it possible to detect obscured objects. Recent approaches in level-set methods incorporate a representation of a reference shape within the energy functional. Thus, the recovered object boundary should resemble the expected contour, in addition to being constrained by length, smoothness and compatibility with the image features. Current work in model-based segmentation using level sets include Leventon [48] Tsai *et al.* [49], Rousson and Paragios [50], Chan [51], Cremers *et al.* [52], and many others. The latest research in constrained deformable modeling deals with multiple different shape templates rather than a single template [53]–[55], with multiple shape instances in a given input image [56], [57] or with the segmentation of temporally evolving shapes [58].

Most methods mentioned above are based on either pixel homogeneity in a region or discontinuity at region boundaries. The homogeneity assumption is rarely the case in practice due to noise. The edge-based methods usually focus on the evolution of object contour. However, as the contour is driven by a local force, the methods are sensitive to local optima due to the lack of a robust stopping criterion. The level set method can be equivalent to the watersnake model by combining level set with Gradient Vector Flow as demonstrated by Xu *et al.* [59].

Both the template based approach and the constrained deformable modeling approach impose rigid and fixed prior shape constraints into the segmentation process. In practice however, the shape constraint may not be rigid and may include some variation. The statistical shape modeling methods [60], [61], [53], [62] can handle variable shape constraints. Primarily represented by the active shape model (ASM) technique developed by Cootes *et al.* [63], the statistical shape modeling is an approach for the incorporation of prior knowledge. The variations

of object shape are estimated by applying principal component analysis to the training samples and a subspace of most influential modes are determined. The restriction of the search for object contours within this subspace can avoid the convergence to irregular shapes. The ASM approach has been successfully used for many tasks in general medical imaging [64]–[66] as well as for segmentation of nerve capillary structures from electron microscope images [67].

The watershed algorithm from mathematical morphology overcomes many drawbacks of the edge-based methods. It is a region-growing algorithm guided by the edge information. It does not assume region homogeneity and it can identify most significant edges between the regions. For watershed-based segmentation, several efforts have been spent on incorporating prior information to the segmentation [1], [68]. Prior knowledge such as information about the number of regions and the location of each region is often provided through markers. Recent work on regularization of the watershed algorithm has mostly focused on imposing smoothness on the watershed lines [1], [69]–[71]. In [72], Vachier and Meyer introduce the viscous watershed transform which can also produce smooth contours by simulating the flooding of viscous fluids like oil and mercury. They prove that the effect of viscous fluids can be achieved with the standard nonviscous watershed algorithm by prefiltering the relief surface with some morphological filters called viscous closing. The method by Grau *et al.* in [71] incorporates prior knowledge into the lower slope used for calculation of topographical distance. In the calculation, the difference between the surface value at two pixels is replaced by the difference between the probability that the pixels belong to the same object class. This probability model can then be defined to carry prior information regarding object appearance features like intensity or color. The latest work by Beare [68] presents a new formulation of the watershed method to impose local smoothness constraint into the watershed lines. The constraint is implemented through a morphological opening operation incorporated into the segmentation process to constrain the borders of regions to be smooth. However, contour smoothness is a too general form of regularization. Shape prior information is much more powerful in representing domain specific knowledge. While the watershed methods above can impose local smoothness, it remains unclear what other boundary constraints can be incorporated. In general, these methods are restricted to local constraints only. Passat *et al.* [73] presented an approach to integrate prior high level anatomical knowledge with 2-D watershed method for brain vessel segmentation. The prior knowledge, however, is primarily used for selecting watershed markers for initialization.

Although incorporation of prior knowledge into segmentation has been well-studied, current methods are either limited to 2-D like most of the constrained energy-based methods or limited to local prior such as the constrained watershed methods. Furthermore, application of prior knowledge to segmentation of cell components from electron tomographic volumes requires further refinements, due to the unique challenges imposed by these data sets. First, the segmentation should allow sufficient flexibility to reflect biological shape variability exhibited by the objects in the volume. Overemphasis of prior knowledge, i.e., rigid size and shape constraints, tends to produce similar segmentations for dissimilar objects, thereby making comparisons among the objects meaningless. Second, given the often non-uniformity of image quality, model-based segmentation needs to be adaptive so that the prior model is weighted more for regions of lower image quality while weighted less for regions of higher image quality. Finally, it is important to perform segmentation in 3-D due to the additional information on feature shape and continuity provided by the 3-D data. In this proposal, we introduce methods to address these issues.

III. Watersnake Segmentation

After carefully studying different possible methods, we introduce a new approach to EM segmentation, which is an extension of the watersnake model [1]. The major contribution is a new combination of energy-based approach with the traditional watershed method, which can incorporate prior information regarding object shape. We call the proposed method shape-driven 3-D watersnake. The choice of the watersnake model is based on the following considerations. First, the watershed algorithm overcomes many drawbacks of the traditional energy-based methods. It is a region growing algorithm guided by the edge information, therefore effectively combining the region information with the edge information, and hence significantly alleviating the local minima problem that has plagued many energy-based methods. In fact, our previous work proves that watersnake can produce a global minimum [1]. In addition, our study shows that compared with the traditional energy-based methods, the watershed method is faster and requires few tuning parameters. Second, Volkmann *et al.* [38] demonstrated the promise of the watershed method for EM image segmentation. Their method, however, remains morphologically based and segmentation is accomplished typically through region growing, without incorporation of any prior information. We want to further improve upon their work by systematically incorporating the local and global prior into the segmentation process so that segmentation can be more accurate and robust for more complex images. Third, despite many weaknesses, one major benefit of the traditional energy-based methods is the mechanism they offer to easily incorporate prior knowledge into the segmentation process. While the traditional watershed algorithm through marker selection can easily impose prior knowledge of the number of objects and their location, it is not convenient for incorporation of priori shape information, especially the global shape information. By reformulating the watershed segmentation in an energy minimization framework, the watersnake model offers a way to combine energy-based approach with the watershed to exploit respective strengths while avoiding their respective weaknesses. In the discussion to follow, we first briefly summarize the watersnake concept [1]. This is then followed by introducing our approach for incorporating local and global priors. Finally, we will discus the extension of the 2-D watersnake to 3-D.

A. Watersnake

Morphologically, the input of a watershed method is a relief function representing edge evidences, where the morphological gradient is the common choice for computing such a relief. By

viewing this function as a mountain landscape, object boundaries are determined as watershed lines. The watershed method is typically implemented with a region growing method, which grows a region from a seed point (marker). To cast the watershed method into an energy minimization framework, we first need to define an energy functional. Let M_i be the seed for each region, and f be the relief function representing the image gradient norm. For any pixel $\mathbf{x}$, we consider the set $[\mathbf{x} \rightsquigarrow M_i]$ of all paths γ linking $\mathbf{x}$ and the marker M_i. The topographical distance from $\mathbf{x}$ to M_i is defined as the minimal sum of gradient norm of f over all possible paths

$$L_i(\mathbf{x}) = \min_{\gamma \in [\mathbf{x} \rightsquigarrow M_i]} \int_{\gamma} |\nabla f| \, ds \tag{1}$$

In our previous work [1], it is proved that a mutually exclusive partition $\Omega_1, \ldots, \Omega_k$ of an image space χ minimizes the energy function

$$E(\Omega_1, \ldots, \Omega_k) = \sum_{i=1}^{k} \iint_{\Omega} \alpha_i + L_i(x) \, dx \tag{2}$$

if and only if the partition is a watershed segmentation of χ. The term α_i is the value f at M_i. Equation (2) establishes the equivalence of the watershed to energy minimization. Details about proof of this theorem can be found in [1]. Details about this theorem can be found in [1]. Besides [1], other works [74]–[80] also discussed combination of watersheds with energy function information.

For this research, we focus on bilayer segmentation, i.e., segmenting one object from a given image. This segmentation divides the image into two regions: the object region and the background region. Furthermore, we assume that the object is a connected region as is usually the case in most applications. The method takes as input two marker regions: M_{out} and M_{int} and a relief function f representing image gradient norm. The exterior marker M_{out} indicates a seed of the background region. Pixels in this marker are known to be background pixels. Similarly, the interior marker M_{in} is a seed of the object region, pixels of which are known to be inside the object. M_{out} and M_{int} can be specified manually or by various automatic algorithms depending on specific applications. Pixels not belonging to any of the markers are referred to as uncertain. The algorithm will determine the segmentation label, either object or background, for uncertain pixels.

Following (2), the watershed between M_{out} and M_{int} is obtained by minimizing the following functional:

$$E(\Omega, \bar{\Omega}) = \iint_{\Omega} L_{\text{in}}(\mathbf{x}) \, d\mathbf{x} + \iint_{\bar{\Omega}} L_{\text{out}}(\mathbf{x}) \, d\mathbf{x} \tag{3}$$

In the subsequent discussion, we will use (3) as the energy function. Compared with the traditional energy-based formulation, the watersnake topographical energy function measures the homogeneity of region Ω. But the topographical energy function does not contain any parameters, a major advantage over the conventional energy terms. The watersnake, therefore, does not need to go back and forth between updating region parameters and updating pixel labels. The minimization is therefore simpler, faster, and less likely to be stuck in the local minimums. In summary, (3) unifies the watershed approach with the energy-based approach. Hence, the watersnake represents a fusion of energy-based segmentation with the morphology-based segmentation, and combine the advantages of both approaches.

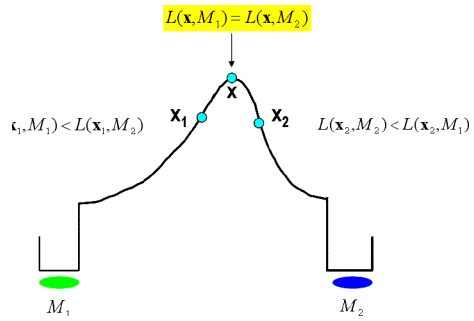

Fig. 2. Illustration of the bilayer watersnake energy function.

B. Incorporation of Prior Information

Having represented the watershed segmentation as an energy minimization, the incorporation of the prior information can be achieved by by adding additional terms to the energy function. Specifically, the labeling of uncertain pixels is obtained by the minimization of an energy function combining a data term, a prior term and a smoothness term

$$E = \alpha E_{\text{data}} + \beta E_{\text{prior}} + \gamma E_{\text{smoothness}} \tag{4}$$

where α, β, and γ are the weighting coefficients. The definition of each term is given subsequently in the remainder of this section.

1) The Data Term: The data term is to help the algorithm locate the object border at the strongest edges between the two markers. Since $\Omega + \bar{\Omega} = \chi$, (3) can be equivalently written as

$$E_{\text{data}}(\Omega) = \iint_{\Omega} [L_{\text{in}}(\mathbf{x}) - L_{\text{out}}(\mathbf{x})] \, d\mathbf{x} \tag{5}$$

over all pixels in region Ω. The border of the Ω that minimizes this functional will be the watershed line where the equality $L_{\text{in}}(\mathbf{x}) = L_{\text{out}}(\mathbf{x})$ is satisfied [77], [81]. Fig. 2 illustrates the bilayer watersnake energy function, where M_i and M_2 are the two seeds for the object and background, respectively.

2) The Fixed Prior Shape Term: This term is meant to impose similarity between the resulting shape and a fixed reference shape, representing the prior knowledge about the feature shape.

Let C_{ref} be the contour of the reference shape and let $D_{\text{ref}}(\mathbf{x})$ be the *signed* distance transform to C_{ref} from $\mathbf{x}$

$$D_{\text{ref}}(\mathbf{x}) = \begin{cases} d(\mathbf{x}, C_{\text{ref}}), & \mathbf{x} \text{ is outside } C_{\text{ref}} \\ -d(\mathbf{x}, C_{\text{ref}}), & \mathbf{x} \text{ is inside } C_{\text{ref}} \end{cases} \tag{6}$$

where $d(\mathbf{x}, C_{\text{ref}})$ denotes the shortest distance from $\mathbf{x}$ to C_{ref}. Since $D_{\text{ref}}(\mathbf{x})$ is negative if and only if $\mathbf{x}$ is inside the reference contour, the region functional $\iint_{\Omega} D_{\text{ref}}(\mathbf{x}) \, d\mathbf{x}$ is minimized if and only if Ω exactly matches the reference shape. Therefore,

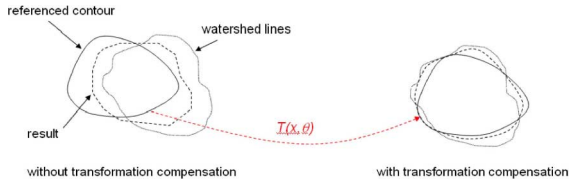

Fig. 3. Fixed prior shape and its transformation to align with the object contour.

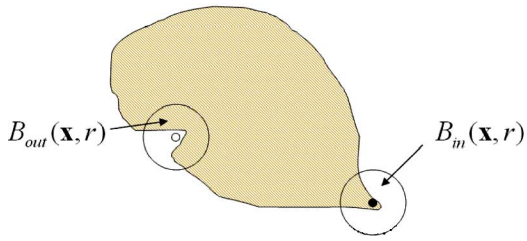

Fig. 4. Illustration of the formulation of the smoothness constraint.

this functional can be added to the energy to constrain Ω to be similar to the reference shape.

Furthermore, to make the minimization result invariant to the position and orientation of the reference shape, we use the transformed distance function. This distance map is obtained from $D_{\text{ref}}(\mathbf{x})$ via a geometrical transformation T with parameters $\boldsymbol{\theta}$.

The fixed prior term is then defined as

$$E_{\text{Fprior}}(\Omega, \boldsymbol{\theta}) = \iint_{\Omega} D_{\text{ref}}(T(\mathbf{x}; \boldsymbol{\theta}))\, d\mathbf{x} \tag{7}$$

where $T(\mathbf{x}; \boldsymbol{\theta})$ denotes the transformation of $\mathbf{x}$. The optimal value of $\boldsymbol{\theta}$ is determined simultaneously with Ω. In this work, we consider the three types of transforms: translation, rotation, and scaling:

$$T(\mathbf{x}; \boldsymbol{\theta}) = \tau \begin{pmatrix} \cos\varphi & -\sin\varphi \\ \sin\varphi & \cos\varphi \end{pmatrix} \begin{pmatrix} x \\ y \end{pmatrix} + \begin{pmatrix} t_x \\ t_y \end{pmatrix} \tag{8}$$

where $\mathbf{x} = (x, y)$ and $\boldsymbol{\theta} = \{\varphi, t_x, t_y, \tau\}$ is the vector of transformation parameters.

Fig. 3 shows the prior shape and its alignment with the object contour.

3) The Variable Prior Term: Unlike the fixed shape prior, the variable shape prior allows certain degree of variability in the prior shape. As we discussed before, this feature is important for EM images since the same structure may vary slightly from tomogram to tomogram.

Following the active shape model proposed by Cootes [63] and Leventon [48], who first proposed the PCA-based shape prior in the pattern recognition field, we formulate the prior shape function as follows. Let $C_1, C_2, \ldots, C_n$ be the training shapes of the biological structure from different tomograms, we can then construct a subspace of those shapes using principal component analysis (PCA)

$$C_{\text{ref}} = C_{\text{mean}} + \sum_{i=1}^{m} \kappa_i U_i \tag{9}$$

where C_{mean} represents the mean shape, U_i are the basis vectors that characterize the main modes of the feature shape variation, and κ_i are the coefficients. Accommodating geometrical transformations T (translation, rotation, scaling), the variable shape regularization term may be rewritten as

$$E_{\text{Vprior}}(\Omega, \theta, \kappa) = \iint_{\Omega} D_{\text{ref}}(T(x; \theta; \kappa))\, dx \tag{10}$$

where $D_{\text{ref}}(x)$ is the distance transform as defined in (7). κ is a vector of κ_i and it is computed together with θ during the optimization such that the search for the shape of object contours is limited to the subspace spanned by U_i.

Note that the representation shape variation using PCA requires the training data set to follow a Gaussian distribution, which implies that the training data have to be globally similar. The PCA method, therefore, cannot represent significant shape variation.

4) The Smoothness Term: This term imposes local smoothness on the contour of Ω. We assume the object boundary locally smooth. The standard approach to producing smoothness is to minimize the contour length, the differentiation of which generates a curvature term in contour evolution equation. In the watersnake framework, however, this approach requires the contour length being implemented as a region functional [1]. In this work, we propose a new smoothness term which is a region functional and at the same time has a similar effect as contour length.

For each pixel $\mathbf{x}$ inside Ω we define $B_{\text{in}}(\mathbf{x}, r)$ as the area of the overlap between a disk of radius r centered at $\mathbf{x}$, and the object exterior $\bar{\Omega}$. Similarly, for each pixel $\mathbf{x}$ outside Ω we define $B_{\text{out}}(\mathbf{x}, r)$ as the area of the overlap between the disk and the object interior, i.e., Ω. Fig. 4 illustrates the smoothness constraint. Let $h(\boldsymbol{x})$ be a mask function that takes values 1 and 0 inside and outside Ω respectively. Then, B_{in} and B_{out} can be expressed as

$$\begin{aligned} B_{\text{in}}(\mathbf{x}, r) &= \int\int_{|\boldsymbol{y}|<r} [1 - h(\boldsymbol{x} + \boldsymbol{y})] d\boldsymbol{x} \\ B_{\text{out}}(\mathbf{x}, r) &= \int\int_{|\boldsymbol{y}|<r} h(\boldsymbol{x} + \boldsymbol{y}) d\boldsymbol{x}. \end{aligned} \tag{11}$$

High values (>0.5) of $B_{\text{in}}(\mathbf{x}, r)$ or $B_{\text{out}}(\mathbf{x}, r)$ on the boundary of Ω indicate high curvatures of the contour. To smooth the contour, we add to the energy a smoothness term defined as

$$\begin{aligned} &E_{\text{smoothness}}(\Omega) \\ &\quad = \iint_{\Omega} \rho(B_{\text{in}}(\mathbf{x}, r)) + \iint_{\bar{\Omega}} \rho(B_{\text{out}}(\mathbf{x}, r)) \end{aligned} \tag{12}$$

where ρ is a function penalizing high values of B_{in} and B_{out}. For example, we have used

$$\rho(e) = \begin{cases} e - B_{\max}(R), & \text{for } e > B_{\max}(R) \\ 0, & \text{otherwise} \end{cases} \tag{13}$$

where $B_{\max}(R)$ is the maximal value of $B_{\text{in}}(\mathbf{x}, r)$ along the border of a digital radius R. As such, the smoothness term becomes effective only when the radius of the osculating circle is less than R.

C. The Total Energy

Based on the above definitions, the total energy function is rewritten as follows if using the fixed prior term

$$E = \iint_{\Omega} \alpha[L_{\text{in}}(\mathbf{x}) - L_{\text{out}}(\mathbf{x})] + \beta D_{\text{ref}}(T(\mathbf{x}; \boldsymbol{\theta}))\, d\mathbf{x} + \gamma \iint_{\Omega} \rho(B_{\text{in}}(\mathbf{x}, r))\, d\mathbf{x} + \gamma \iint_{\Omega} \rho(B_{\text{out}}(\mathbf{x}, r))\, d\mathbf{x} \quad (14)$$

or is written as follows if the variable prior term is used

$$E = \iint_{\Omega} \alpha[L_{\text{in}}(\mathbf{x}) - L_{\text{out}}(\mathbf{x})] + \beta D_{\text{ref}}(T(\mathbf{x}; \boldsymbol{\theta}; \boldsymbol{\kappa}))\, d\mathbf{x} + \gamma \iint_{\Omega} \rho(B_{\text{in}}(\mathbf{x}, r))\, d\mathbf{x} + \gamma \iint_{\Omega} \rho(B_{\text{out}}(\mathbf{x}, r))\, d\mathbf{x} \quad (15)$$

Given the total energy function, the force acting on a point x at the border of a region consists of forces from different sources as represented by the different terms in the functional. The PDE of this functional can then be used to determine the motion of the boundary.

Without changing the minimization solution, we fix the value of $\alpha = 0.5$ and tune β and γ for specific applications. Below we will discuss an automatic method to adaptively vary β and γ, depending on image quality.

D. Locally Adaptive Weights

Noise in electron tomographic volumes of objects such as mitochondria poses a challenge for automatic segmentation. While images are often cluttered with many irrelevant details, object data may be weak or absent at some places where the object is dense and penetration of the electron beam is poor. When unstained frozen-hydrated specimens are used, resulting images usually have low contrast. These factors together with limited angular sampling and an incomplete tilt range lead to low SNR and directional resolution loss in some portion of the tomogram. We observe that the proposed method has difficulty with detecting object borders at low contrast regions or regions that are highly textured with clutter. In such regions, it is better to rely more on the prior shape model. This observation allows us to design a method to make β adaptive to local photometric characteristics such that in the area where the watershed line may be inaccurate we like to rely more on the prior by increasing the value β.

To characterize image textures in the neighborhood $\mathcal{N}$ of a pixel $\boldsymbol{x}$, we put all gradient vectors of pixels in $\mathcal{N}$ in the same coordinate system with $\boldsymbol{x}$ being the origin. We then fit the end points of the vectors into an ellipsoid via eigenvector decomposition. The three axes of this ellipsoid can be obtained from the eigenvalues of the following matrix:

$$F = \begin{pmatrix} \sum_{\mathcal{N}} I_x I_x & \sum_{\mathcal{N}} I_x I_y & \sum_{\mathcal{N}} I_x I_z \\ \sum_{\mathcal{N}} I_y I_x & \sum_{\mathcal{N}} I_y I_y & \sum_{\mathcal{N}} I_y I_z \\ \sum_{\mathcal{N}} I_z I_x & \sum_{\mathcal{N}} I_z I_y & \sum_{\mathcal{N}} I_z I_z \end{pmatrix} \quad (16)$$

where I_x, I_y, and I_z denote the image derivative with respect to x, y, z, respectively. Let $\lambda_{\min}$ and $\lambda_{\max}$ be the minimum and maximum eigenvectors of F respectively and consider their ratio

$$\varsigma = \frac{\lambda_{\min}}{\lambda_{\max}}. \quad (17)$$

Low values of ς indicate that all gradient vectors in $\mathcal{N}$ are strongly oriented and $\boldsymbol{x}$ is close to a clear edge where the watershed is expected to produce an accurate result. On the other hand, high values of ς (close to 1) indicate either a homogeneous region or a highly noisy region where the gradient vectors are diffused. In this case, the watershed often does not produce accurate results. Thus, the prior weight can be set as:

$$\beta \propto (1 + c\varsigma) \quad (18)$$

where c is a constant.

In addition, β should also be adaptive to the distance between the watershed line and the reference contour. If the watershed line is too far from the reference contour, a high weigh for D_{ref} [defined in (6)] should be used. But when the watershed is close to the reference contour, a small weigh of D_{ref} should be used, leaving the resulting contour close to the watershed line which better adheres to edges. To incorporate the closeness to the reference contour we can set

$$\beta \propto \eta(D_{\text{ref}}) \quad \text{where} \quad \eta(D_{\text{ref}}) = \begin{cases} 0.8 & |D_{\text{ref}}| \geq 5 \\ 0.1 & |D_{\text{ref}}| < 5 \end{cases} \quad (19)$$

Combining all above three considerations, we set β as follows:

$$\beta = \beta_0(1 + c\varsigma)\eta(D_{\text{ref}}) \quad (20)$$

where β_0 is a predefined constant.

E. Extension to 3-D

All energy terms of the proposed framework are readily for extension to the 3-D case. Given a 3-D image $I(x, y, z)$ we can calculate its morphological gradient f at each pixel as the difference between the maximum and the minimum of I in a neighborhood of the pixel. Given two marker sets M_{in} and M_{out}, the 3-D watershed segmentation can be obtained by minimizing

$$\min_{\Omega} \iint_{\Omega} [\mathcal{L}_{\text{in}}(\mathbf{x}) - \mathcal{L}_{\text{out}}(\mathbf{x})]\, d\mathbf{x} \quad (21)$$

where $\mathcal{L}$ denotes the 3-D topographical distance. A fixed prior shape can also be incorporated by adding to the watershed energy a volume integral of distance to a reference 3-D surface

$$\min_{\Omega,\theta} \iiint_{\Omega} \alpha[\mathcal{L}_{\text{int}}(\mathbf{x}) - \mathcal{L}_{\text{ext}}(x\mathbf{x})] + \beta D_{3\text{ref}}(T(\mathbf{x}, \theta))dx \quad (22)$$

where $D_{3\text{ref}}$ is the 3-D distance transform function defined similarly as in (7). The variable prior and the smoothness terms can be extended to the 3-D in a similar fashion.

F. Minimization Algorithm

As will be shown, the minimization of the smoothness term requires much computation. Therefore, we first minimize $E_{\text{data}}(\Omega) + E_{\text{prior}}(\Omega, \theta)$[1] with respect to Ω and θ. The resulting segmentation will be used as the initial point for the minimization of the total energy $E_{\text{data}} + E_{\text{prior}} + E_{\text{smoothnes}}$ with respect to Ω.

1) Minimization of $\alpha E_{\text{data}}(\Omega) + \beta E_{\text{prior}}(\Omega, \theta)$ can be carried out as follows:
   a) Given an initial estimate of θ.
   b) Fixing θ, determine Ω by selecting all pixels where the integrand is negative

$$\Omega = \{\mathbf{x} | \alpha[L_{\text{in}}(\mathbf{x}) - L_{\text{out}}(\mathbf{x})] + \beta D_{\text{ref}}(T(\mathbf{x}; \theta)) < 0\}. \quad (23)$$

   c) Fixing Ω, optimize for transformation parameters θ:

$$\min_{\theta} \iint_{\Omega} D_{\text{ref}}(T(\mathbf{x}; \boldsymbol{\theta}))\, d\mathbf{x}. \quad (24)$$

   d) Iterate Steps 2 and 3 until stability.

   The minimization in (24) is done by the exhaustive search in a neighborhood of the previous estimate of θ.
2) Minimization of full energy $E = \alpha E_{\text{data}} + \beta E_{\text{prior}} + \gamma E_{\text{smoothness}}$.
   a) Start from the segmentation result of the previous algorithm.
   b) For each pixel $\boldsymbol{x}$ at object border, calculate $\nabla E(\boldsymbol{x})$, the decrease of the energy function for the case where the label of the pixel is changed. Specifically, when the pixel is changed from "background" to "object"

$$\begin{aligned}\Delta^{+} E(\boldsymbol{x}) &= \alpha[L_{\text{in}}(\mathbf{x}) - L_{\text{out}}(\mathbf{x})] + \beta D_{\text{ref}}(T(\mathbf{x}; \theta)) \\ &\quad + \sum_{\mathbf{y} \in \Omega, |\mathbf{y} - \boldsymbol{x}| < r} [\rho(B_{\text{in}}(\mathbf{y}, r) - 1) - \rho(B_{\text{in}}(\mathbf{y}, r))] \\ &\quad + \sum_{\mathbf{y} \notin \Omega, |\mathbf{y} - \boldsymbol{x}| < r} [\rho(B_{\text{in}}(\mathbf{y}, r) + 1) - \rho(B_{\text{in}}(\mathbf{y}, r))]\end{aligned} \quad (25)$$

   On the other hand, if the pixel is changed from "object" to "background," the energy decrease is calculated as

$$\begin{aligned}\Delta^{-} E(\boldsymbol{x}) &= -\alpha[L_{\text{in}}(\mathbf{x}) - L_{\text{out}}(\mathbf{x})] - \beta D_{\text{ref}}(T(\mathbf{x}; \theta)) \\ &\quad + \sum_{\mathbf{y} \in \Omega, |\mathbf{y} - \boldsymbol{x}| < r} [\rho(B_{\text{in}}(\mathbf{y}, r) + 1) - \rho(B_{\text{in}}(\mathbf{y}, r))] \\ &\quad + \sum_{\mathbf{y} \notin \Omega, |\mathbf{y} - \boldsymbol{x}| < r} [\rho(B_{\text{in}}(\mathbf{y}, r) - 1) - \rho(B_{\text{in}}(\mathbf{y}, r))].\end{aligned} \quad (26)$$

[1]For simplicity, we only consider the fixed shape prior here.

   c) Select pixel with the maximal potential decrease of the energy. Denote it $\boldsymbol{x}_m$.
   d) If $\Delta E(\boldsymbol{x}_m) < 0$ then stop.
   e) Otherwise, recompute the potential energy decrease ∇E for all border pixels within a $2r$ distance from $\boldsymbol{x}_m$.
   f) Iterate Steps 3–5.

As observed, the computation of $\Delta E(\boldsymbol{x})$ is an expensive operation requiring a scan over the neighborhood of $\boldsymbol{x}$. In addition, the need to recompute ∇E for border pixels in the neighborhood $\boldsymbol{x}_m$ makes the optimization with the smoothness term computationally expensive.

G. Acquisition of the Prior Shape

An important part of the proposed research is to capture the prior shape of the biological features. The acquisition of prior knowledge about the shape of structures will be carried out interactively with the user. For structures with parameterizable shapes such as mitochondrial or bacterial outer membrane boundaries and some crista junctions with regular shapes [6], it should be possible to parameterize these membrane segments as either cylinders or hyperboloids of revolution. Given the parametric models, the user is asked to select a few points on the surface of the structure. The program uses these points along with the parametric model to obtain estimates of the shape parameters, which in turn, are fed into the segmentation software to perform the segmentation.

For more complicated structures that cannot be characterized analytically but which have relatively consistent shapes across different volumes, a set of training datasets (tomograms) is needed to capture the mean shape of the structure and its random variability across volumes following (9). The user is asked to manually map out points on a typical structure in each volume either in 2-D or 3-D, producing a cloud of 3-D points representing the surface of the structure. This is then repeated for different volumes, producing sets of 3-D points. The mean and covariance matrix of the sets of 3-D points are then acquired. The covariance matrix captures the random variability of structure across different volumes, which is fed into the segmentation software. Observed variability in the crista junctions of isolated rat liver mitochondria (see Fig. 1), in terms of length and flattening, would present a good test of the ability of the segmentation algorithms to deal with random variation in structures.

Finally, there are structures inside cells that are both complicated and vary significantly from volume to volume, with no obvious common shape at any scale. In these cases, the user will be asked to provide a set of control points on the surface of the feature of interest in every volume to be segmented. The program will then perform segmentation subject to the constraint that the final surface must go through the manually identified points. Provided the control points are good, the end product would be an accurate and objectively defined surface.

In general, to overcome the difficulty of specifying the 3-D shape manually, we adopt the following procedure. We assume as given only a few 2-D contours which are the intersection of

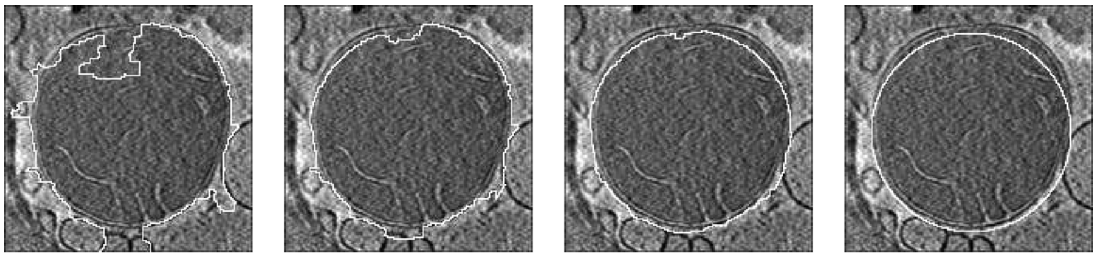

Fig. 5. Results of the proposed algorithm for different weights of the shape prior term.

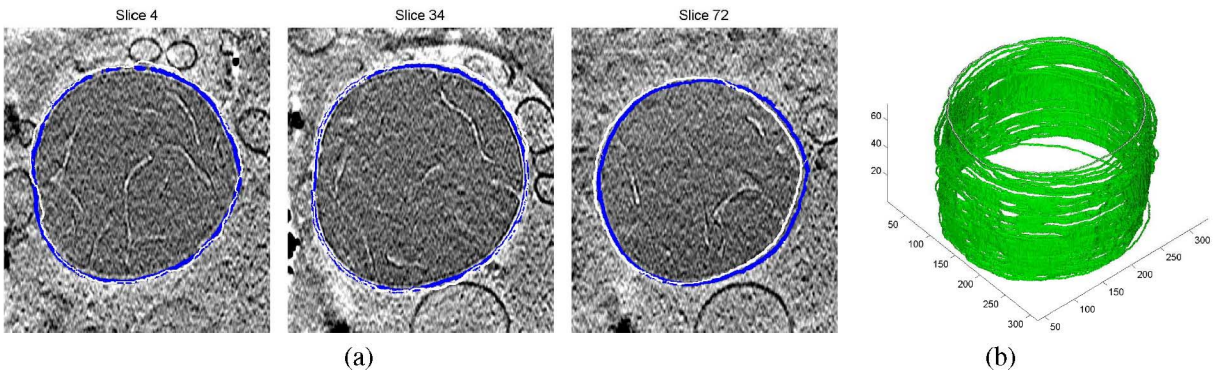

Fig. 6. Results from the 2-D version of the proposed watersnake algorithm with incorporation of reference shape and smoothness. (a) White contours represent the result of the proposed algorithm. Dark (or blue) contours are the manual segmentation provided by an expert. (b) Three-dimensional surface obtained by stacking the white contours of all slices.

the reference surface with certain z slices. Information about the reference surface in between the slices is obtained by linear interpolation. Specifically, suppose C_1 and C_2 be the reference contours given for two different slices of the reference surface. We compute the signed distance transforms of these contours and denote them $d(x, C_1)$ and $d(x, C_2)$, respectively. The reference contour C of a slice in between C_1 and C_2 is determined as set of points satisfying

$$\nu d(x, C_1) + (1 - \nu) d(x, C_2) = 0 \tag{27}$$

where ν is a weighting coefficient calculated based on the relative position of the slice to C_1 and C_2. Let z, z_1, and z_2 be the z value of the slices that contain C, C_1, and C_2, respectively. Then

$$\nu = \frac{|z - z_1|}{|z_2 - z_1|}. \tag{28}$$

IV. Experiments

To demonstrate the promise of our methods on EM images, we first applied them to tomograms of intact frozen-hydrated rat liver mitochondria for the segmentation of outer membranes. In this case, the outer membrane is only 10 nm from the inner membrane at the organelle periphery. For the experiments, before the segmentation started, images are fisrt smoothed by the opening by reconstruction filter [42]. The exterior marker is specified as a rectangle enclosing the object of interest, while the interior marker is specified as a point inside the object. The coefficient α is fixed at 0.5. Other than Fig. 5, β_0 for volumes in other figures are all set to 0.3. For the computation of ρ, we used $R = 20$ and $r = 20$. The coefficient γ is set to a large value 500 which effectively removes all sharp corners for which the radius of the osculating disk is less than R. The coefficient β is calculated as follows. Once the two topographic distance L_{in} and L_{out} have been computed, the original watershed contour can be determined. We then calculate the mean $\bar{f}$ of the gradient values along the watershed line, and set

$$\beta = \frac{\beta_0}{\bar{f}}. \tag{29}$$

Such setting of β will makes the result of the minimization invariant to scaling of image intensity.

Fig. 5 shows the result of the proposed algorithm for the segmentation of a 2-D mitochondria image obtained from one slice in a 3-D tomography volume. The task was to segment the outer membrane of the mitochondria structure. The image is very noisy and cluttered. The reference shape is chosen as a circle. The result with incorporation of the reference shape shows an obvious improvement over the original watershed lines which has several excursions of the contour into the object or background regions. Moreover, changing the weighting coefficient of the shape term leads to smooth transition from the result of the original watershed algorithm to a result that looks the same as the reference shape.

We first study the 2-D version of the proposed method (i.e., perform segmentation on each slice). Fig. 6 shows the segmentation results of different slices in a 3-D mitochondria tomography image volume. The volume has 74 slices.

The reference shape was selected by manually segmenting the outer membrane of one of the slices. The reference looks

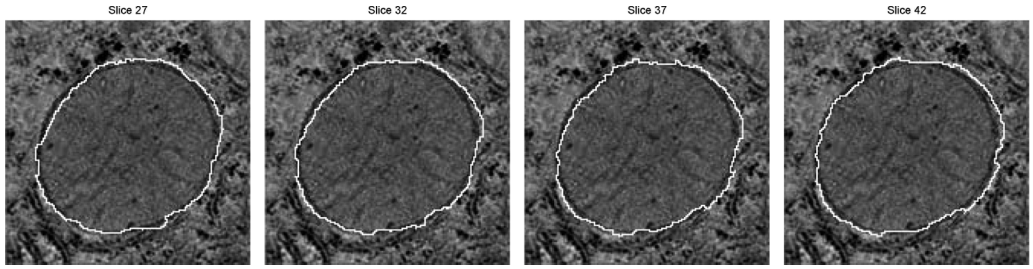

Fig. 7. Result of the proposed 2-D watersnake with incorporation of prior shape knowledge for another mitochondria EM image.

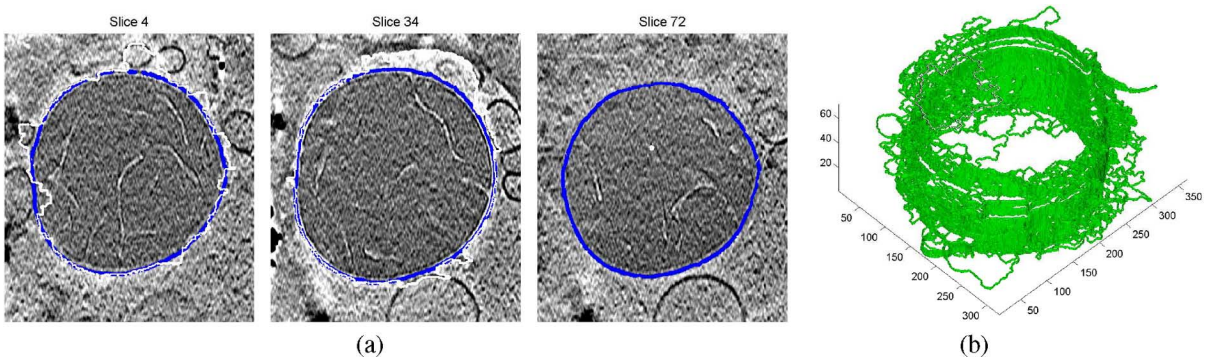

Fig. 8. Results of the original 2-D watershed algorithm without any constraint. Segmentation fails for slice 72.

exactly as the rightmost image in Fig. 5. Since the membranes at the first and the last slices are significantly smaller than the slices in the middle, we used three different reference shapes for different parts of the volume. Specifically, for segmenting slices 20–59 we used the manual segmentation of slice 30, for slices 1–19 and slices 60–74 the manually segmentation of slice 10 and 70 were used as reference, respectively. For evaluation, we also show the contour manually drawn by an expert. The results of the individually computed contours are then stacked to form a 3-D surface that is shown in Fig. 6(b).

Fig. 7 shows the results of the proposed algorithm for another volume image. As observed, the results are generally accurate although errors are still observed at few places due to dark particles that create high peaks on the gradient surface.

For comparison, the results of the original 2-D watershed algorithm is shown in Fig. 8. As expected, the watershed algorithm failed to identify the correct membrane boundaries due to its sensitivity to image clutter. In slice 72, the contour even shrinks to a small dot. The poor performance is further demonstrated by the 3-D rendering of the 2-D detection as shown in the bottom two figures.

To study the performance of the 3-D version of the proposed method, for the same sequence we then applied our 3-D watershed algorithm. A reference surface was created from five reference contours specified for slices 1, 10, 30, 50, and 74, respectively. During energy minimization, we do not consider the full 3-D geometrical transformation of the reference volume but only the translation and rotation in the (x, y) plane. Two 3-D markers are obtained by stacking the 2-D markers of all slices, yielding a vertical line for the interior marker and a rectangular tube for the exterior marker. The results are shown in Fig. 9. The generated contours closely follow the manually drawn contours. it is clearly that by taking advantage of the 3-D information, the 3-D watersnake outperforms the 2-D watersnake, despite the use of the same amount of prior shape information. In fact, the 3-D watersnake is better than its 2-D counterpart with or without shape prior. In addition, the results by 3-D watersnake are also much better than the results of the 3-D watershed algorithm, which are shown in Fig. 10. This demonstrates the importance of the prior information. Hence, it is important to use both 3-D data and prior shape information for robust and accurate segmentation. The proposed algorithm can segment membranes in volume image of size $400 \times 400 \times 100$ in just a few minutes on a 1.4-GHz laptop.

To further demonstrate the proposed method, we applied it to segment both the inner and outer membrane boundaries. Fig. 11 shows the results for the inner and outer membrane boundaries in the cell wall of a specially prepared (focused ion beam (FIB)-milled) E. coli bacterium. During segmentation, the user manually traced a few slices, based on which a 3-D reference shape model was constructed. To detect both the inner and outer membrane boundaries, we first detected the outer membrane and then used it as the outer marker of the second run of the algorithm, which returned the inner membrane.

We have quantitatively evaluated the performance of the proposed approach using the manually drawn contours as the groundtruth. For this purpose, we have used two statistics: precision and recall (corresponding to specificity and sensitivity, respectively). The precision is the percentage of machine-generated boundary pixels that are true boundary pixel. The recall is the percentage of true boundary pixels that are detected by the algorithm. The results are summarized in Table I. The reason that the recall is lower than the precision in the above table is that the ground truth boundary is thicker than the machine-generated contour which has only one pixel thickness. As observed, the 3-D watershed with incorporation

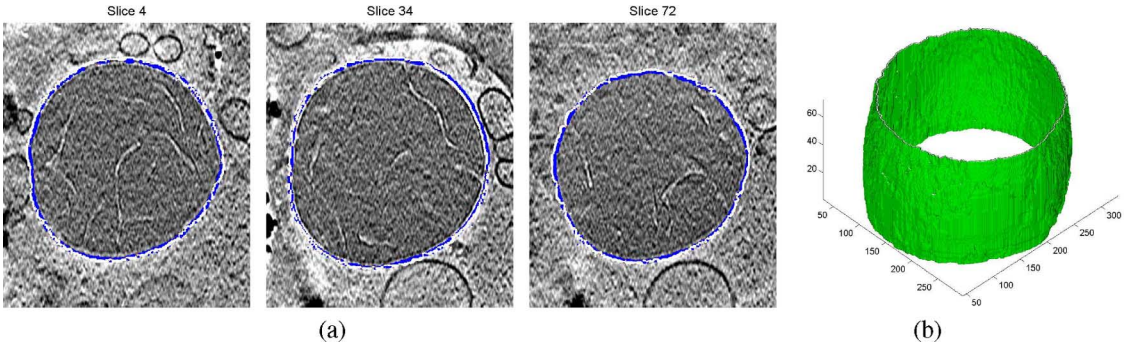

Fig. 9. Result of 3-D watershed with incorporation of a reference 3-D shape. (a) White contours represent the result of the proposed algorithm. Dark (or blue) contours are the manual segmentation provided by an expert. (b) Three-dimensional surface obtained by stacking the white contours of all slices. White contours apparently closely follow the dark contours.

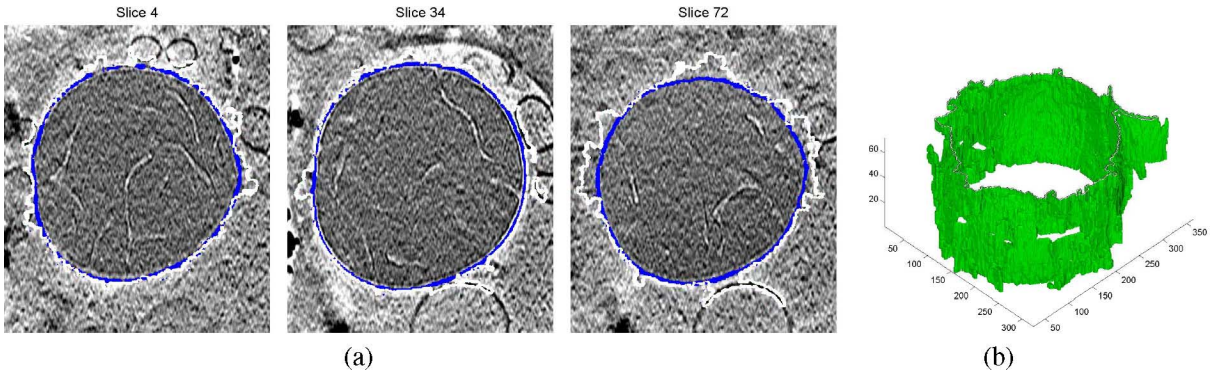

Fig. 10. Result of 3-D watersnake without prior knowledge.

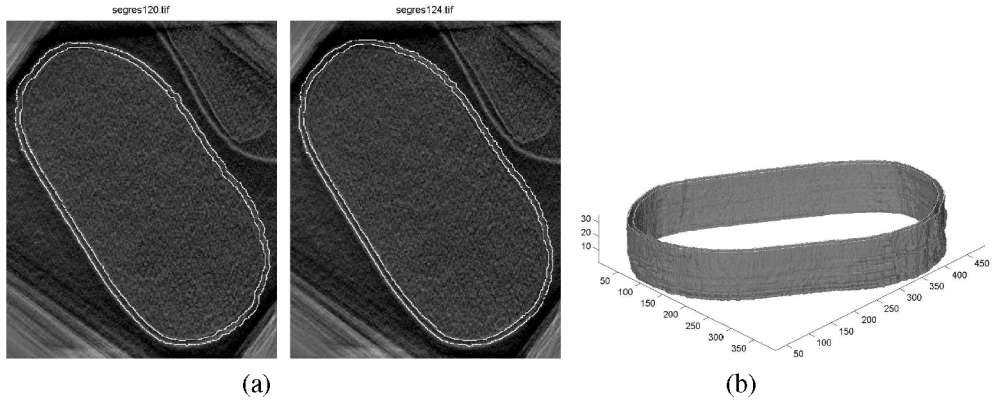

Fig. 11. Detection of closely spaced double membranes using the proposed 3-D watersnake. (a) Detection results in 2-D and (b) Detection results in 3-D. Bacterium is 800 nm in diameter, milled to a thickness of 400 nm; the spacing between membranes is 30 nm.

TABLE I
RESULTS OF QUANTITATIVE EVALUATION FOR DIFFERENT SEGMENTATION SETTINGS

setting	precision	recall
2D original watershed	0.47	0.47
2D watershed with prior shape	0.69	0.52
2D watershed with prior shape and smoothness	0.70	0.52
3D original watershed	0.50	0.55
3D watershed with prior shape	0.95	0.70

of a reference shape has the best performance while the original 2-D watershed has the poorest performance.

V. CONCLUSION

In this paper, we introduce mathematical solutions for model-based automatic segmentation in electron tomography. In particular, we propose to segment and trace biological membranes. Based on combining two powerful segmentation approaches (energy-based and watershed), the proposed method inherits each approach's strengths while avoiding their weaknesses. In addition, the systematic incorporation of both global and local prior knowledge into the segmentation process as well as the extension of the segmentation from 2-D to 3-D further enhance the capabilities of the proposed method for difficult and complex EM images. The promise of the methods

are demonstrated for automatically segmenting biomedical membranes of a globally convex shape. Specifically, experiments demonstrate the importance and significance of prior shape and the 3-D information in improving segmenting and tracing difficult biological membranes. In the future, we will extend the proposed methods for segmenting more complex membranes, such as mitochondrial inner membrane cristae and their junctions.

While the focus of the proposed research is on segmentation of biological membranes in EM images, the proposed techniques will have wide applicability to other cellular structures in electron tomography and to other forms of medical imaging, since the underlying theories of combining prior knowledge with image data remains true with other features. In addition, the proposed research may also be applicable to other modalities such as MRI and ultrasound since the quality of those modalities are at least as good, and usually better than EM images.

ACKNOWLEDGMENT

The authors would like to thank Dr. C. Renken and Dr. C. Mannell from Wadsworth Center for many stimulating discussions on the work described in this paper, and for providing us with the electron tomography data. The authors would also like to express our appreciation to the anonymous reviewers for many of their insightful, constructive, and very detailed comments. These comments help greatly improve this manuscript.

REFERENCES

[1] H. Nguyen, M. Worring, and R. van den Boomgaard, "Watersnakes: Energy-driven watershed segmentation," *IEEE Trans. Pattern Anal. Mach. Intell.*, vol. 25, no. 3, pp. 330–342, Mar. 2003.

[2] B. F. McEwen and M. Marko, "The emergence of electron tomography as an important tool for investigating cellular ultrstructure," *J. Histochem. Cytochem.*, vol. 49, no. 7, pp. 553–563, 2001.

[3] R. McIntosh, D. Nicastro, and B. Mastronarde, "New views of cells in 3-D: An introduction to electron tomography," *Trends Cell Biol.*, vol. 15, pp. 43–51, 2005.

[4] C. A. Mannella, M. Marko, and K. Buttle, "Reconsidering mitochondrial structure: New views of an old organelle," *Trends Biochem. Sci.*, vol. 22, pp. 37–38, 1997.

[5] C. A. Mannella, D. R. Pfeiffer, P. C. Bradshaw, I. I. Moraru, B. Slepchenko, L. M. Loew, C. Hsieh, K. Buttle, and M. Marko, "Topology of the mitochondrial inner membrane: Dynamics and bioenergetic implications," *IUBMB Life*, vol. 52, pp. 93–100, 2001.

[6] G. Perkins, C. Renken, M. E. Martone, S. J. Young, M. Ellisman, and T. Frey, "Electron Tomography of Neuronal Mitochondria : Three-Dimensional Structure and Organization of Cristae and Membrane Contacts," *J. Structural Biol.*, pp. 260–272, 1997.

[7] T. Frey and C. A. Mannella, "The internal structure of mitochondria," *Nature*, vol. 409, pp. 479–484, 2000.

[8] B. J. Marsh, D. N. Mastronarde, K. F. Buttle, K. E. Howell, and J. R. McIntosh, "Organellar relationships in the golgi region of the pancreatic beta cell line, hit-t15, visualized by high resolution electron tomography," *Proc. Nat. Acad. Sci. USA*, vol. 98, pp. 2399–2406, 2001.

[9] M. L. Harlow, D. Ress, A. Stoschek, M. Marshall, and U. J. McMahan, "The architecture of active zone material at the frog's neuromuscular junction," *Nature*, vol. 409, pp. 479–484, 2001.

[10] J. R. Kremer, D. N. Mastronarde, and J. R. McIntosh, "Computer visualization of three dimensional image data using imod," *J. Struct. Biol.*, vol. 116, pp. 71–76, 1996.

[11] J. Frank, M. Radermacher, P. Penczek, J. Zhu, Y. Li, M. Ladjadj, and A. Leith, "Spider and web: Processing and visualization of images ion 3-D electron microscopy and related fields," *J. Struct. Biol.*, vol. 116, pp. 190–199, 1996.

[12] M. Marko and A. Leith, "Sterecon-three-dimensional reconstructions from stereoscopic contouring," *J. Struct. Biol.*, vol. 116, pp. 93–98, 1996.

[13] W. Rasband and D. Bright, "NIH image," *Microbeam Anal.*, vol. 4, pp. 20–33, 1995.

[14] D. Hessler, S. J. Young, and M. H. Ellisman, "A flexible environment for the visualization of three-dimensional biological structures," *J. Struct. Biol.*, vol. 116, pp. 113–119, 1996.

[15] Y. Li, A. Leith, and J. Frank, "Tinkerbell—A tool for interactive segmentation of 3-D data," *J. Struct. Biol.*, vol. 120, pp. 266–275, 1997.

[16] J. Segui-Simarro, J. Austin, E. White, and L. Staehelin, "Electron tomographic analysis of somatic cell plate formation in meristematic cells of arabidopsis preserved by high-pressure freezing," *Plant Cell*, vol. 16, pp. 836–856, 2004.

[17] G. Sosinsky, T. Deerinck, R. Greco, C. Buitenhuys, T. Bartol, and M. Ellisman, "Development of a model for microphysiological simulations: Small nodes of ranvier from peripheral nerves of mice reconstructed by electron tomography," *Neuroinformatics*, vol. 3, pp. 133–162, 2005.

[18] B. J. Marsh, A. J. Costin, J. P. Morgan, and P. van der Heide, "3-D structure studies of the pancreatic beta cell by high resolution electron microscope (em) tomography," *Microsc. Microanal.*, vol. 11, pp. 326–327, 2005.

[19] S. Osher and J. A. Sethian, "Fronts propagating with curvature dependent speed: Algorithms based on Hamilton-Jacobi formulations," *J. Computational Phys.*, vol. 79, pp. 12–49, 1988.

[20] R. Noumeir and R. El-Daccace, "Attenuation correction in spect using active surfaces," in *IEEE Nucl. Sci. Symp. Med. Imag. Conf.*, 1999, vol. 3, pp. 1995–1999.

[21] E. A. Ashton, K. J. Parker, M. J. Berg, and C. W. Chen, "A novel volumetric feature extraction technique with applications to MR images," *IEEE Trans. Med. Imag.*, vol. 16, no. 4, pp. 365–371, Aug. 1997.

[22] J. Snell, M. Merickel, J. Ortega, and J. Goble, "Model based boundary estimation of complex objects using hierarchical active surface templates," *Pattern Recognit.*, vol. 28, pp. 1599–1609, 1995.

[23] T. McInerny and D. Terzopoulos, "Deformable models in medical image analysis: A survey," *J. Math. Imag. Vision*, vol. 23, no. 1, pp. 67–86, 2005.

[24] A. Bartesaghi, G. Sapiro, and S. Subramaniam, "An energy-based three dimensional segmentation approach for the quantitative interpretation of electron tomograms," *IEEE Trans. Image Process.*, vol. 14, no. 9, pp. 1314–1323, Sep. 2005.

[25] S. Babu, P. C. Liao, M. C. Shin, and L. V. Tsap, "Towards recovery of 3-D chromosome structure," in *IEEE Workshop Articulated Nonrigid Motion ANM2004 (in Conjunction with CVPR'04)*, 2004, vol. 1, p. 1.

[26] B. Appleton and H. Talbot, "Globally optimal geodesic active contours," *Math. Imag. Vis.*, 2005.

[27] M. Jacob, T. Blu, and M. Unse, "3-D reconstruction of DNA filaments from stereo cryo-electron micrographs," in *Proc. 2002 IEEE Int. Symp. Biomed. Imag.*, 2002, pp. 597–600.

[28] J. A. Sethian, *Level Set Methods and Fast Marching Methods*, 2nd ed. Cambridge, U.K.: Cambridge Univ. Press, 1999.

[29] C. Bajaj, Z. Yu, and M. Auer, "Volumetric feature extraction and visualization of tomographic molecular imaging.," *J. Struct. Biol.*, vol. 144, pp. 132–143, 2003.

[30] A. S. Frangakis and R. Hegrel, "Segmentation of two and three dimensional data from electron microscopy using eigenvector analysis," *J. Struct. Biol.*, vol. 138, pp. 105–113, 2002.

[31] J. Shi and J. Malik, "Normalized cuts and image segmentation," *IEEE Trans. Pattern Anal. Mach. Intell.*, vol. 22, no. 8, pp. 888–905, Aug. 2000.

[32] L. Cohen and R. Kimmel, "Global minimum for active contours models: A minimal path approach," *Int. J. Comput. Vis.*, vol. 24, no. 1, pp. 57–78, 1997.

[33] T. Chan and L. Vese, "Active contours without edges (acwe)," *IEEE Trans. Image Process.*, vol. 10, no. 2, pp. 266–277, Feb. 2001.

[34] L. Vincent and P. Soille, "Watershed in digital spaces: An efficient algorithm based on immersion simulations," *IEEE Trans. Pattern Anal. Mach. Intell.*, vol. 13, no. 6, pp. 583–598, Jun. 1991.

[35] S. Beucher and F. Meyer, , E. Dougherty, Ed., "The morphological approach of segmentation: The watershed transformation," in *Mathematical Morphology in Image Processing*. New York: Marcel Dekker, 1992, ch. 12, pp. 433–481.

[36] F. Meyer, "An overview of morphological segmentation," *Int. J. Pattern Recognit. Artif. Intell.*, vol. 15, no. 7, pp. 1089–1118, 2001.

[37] F. Meyer, , M. Bilodeau, F. Meyer, and M. Schmitt, Eds., "Morphological segmentation revisited," in *Space, Structure and Randomness—Contributions in Honor of Georges Matheron in the Fields of Geostatistics, Random Sets, and Mathematical Morphology*. : Springer, 2005, vol. 183, Lecture Notes in Statistics, pp. 315–347.

[38] N. Volkmann, "A novel three dimensional variant of the watershed transform for segmentation of electron display maps," *J. Struct. Biol.*, vol. 138, pp. 123–129, 2002.
[39] B. J. Marsh, N. Volkmann, J. R. McIntosh, and K. E. Howell, "Direct continuities between cisternae at different levels of the golgi complex in glucose-stimulated mouse islet beta cells," *Proc. Nat. Acad. Sci. USA*, vol. 101, pp. 5565–5570, 2004.
[40] C. A. Mannella, "The relevance of mitochondrial membrane topology to mitochondrial function," *Biochim. Biophys. Acta: Molec. Basis Disease*, pp. 140–147, 2005.
[41] C. A. Mannella, M. Marko, P. Penczek, D. Barnard, and J. Frank, "The internal compartmentation of rat-liver mitochondria: Tomographic study using the high-voltage transmission electron microscope," *Microscopy Res. Tech.*, vol. 27, pp. 278–283, 1994.
[42] P. Soille, *Morphological Image Analysis: Principles and Applications*, 2nd ed. Berlin, Germany: Springer-Verlag, 2003.
[43] B. Naegel, "Using mathematical morphology for the anatomical labeling of vertebrae from 3-D CT-scan images," *Computerized Medical Imag. Graphics*, vol. 31, no. 3, pp. 141–156, 2007.
[44] J. Bohm, A. S. Frangakis, R. Hegerl, S. Nickell, D. Typke, and W. Baumeister, "Toward detecting and identifying macromolecules in a cellular context: Template matching applied to electron tomograms," *Proc. Nat Acad. Sci. USA*, vol. 97, pp. 14245–14250, 2000.
[45] J. Frank and T. Wagenkenecht, "Automatic selection of molecular images from electron micrographs," *Ultramicroscopy*, vol. 12, pp. 169–176, 1984.
[46] A. S. Frangakis, J. Bohm, F. Forster, S. Nickell, D. Nicastro, D. Typke, R. Hegerl, and W. Baumeister, "Identification of macromolecular complexes in cryoelectron tomograms of phantom cells," *Proc. Nat Acad. Sci. USA*, vol. 99, pp. 14153–14148, 2002.
[47] B. K. Rath, R. Hegerl, A. Leith, T. R. Shaikh, T. Wagenknecht, and J. Frank, "Fast 3-D motif search of EM density maps using a locally normalized cross-correlation function," *J. Struct. Biol.*, vol. 144, pp. 95–103, 2003.
[48] M. Leventon, O. Faugeras, E. Grimson, and W. Wells, "Level set based segmentation with intensity and curvature priors," *Math. Methods Biomed. Image Anal. (MMBIA)*, 2000.
[49] A. Tsai, A. Yezzi, Jr., W. Wells, III, C. Tempany, D. Tucker, A. Fan, W. Grimson, and A. Willsky, "Model-based curve evolution technique for image segmentation," in *Proc. IEEE Conf. Comp. Vis. Pattern Recognit.*, 2001, pp. I: 463–I: 468.
[50] M. Rousson and N. Paragios, "Shape priors for level set representations," in *Proc. Eur. Conf. Comput. Vis.*, 2002, p. II.
[51] T. Chan and W. Zhu, "Level set based shape prior segmentation," in *Proc. IEEE Conf. Comp. Vis. Pattern Recognit.*, 2005, pp. II: 1164–II: 1170.
[52] D. Cremers, F. Tischhauser, J. Weickert, and C. Schnorr, "Diffusion snakes: Introducing statistical shape knowledge into the Mumford-Shah functional," *Int. J. Comput. Vis.*, vol. 50, pp. 295–313, 2002.
[53] M. Leventon, E. Grimson, and O. Faugeras, "Statistical shape influence in geodesic active contours," in *Proc. IEEE Conf. Comp. Vision Pattern Recognit.*, 2000, pp. 1316–1323.
[54] D. Cremers, S. J. Osher, and S. Soatto, "Kernel density estimation and intrinsic alignment for shape priors in level set segmentation," *Int. J. Comput. Vis.*, vol. 69, no. 3, pp. 335–351, 2006.
[55] M. Rousson, N. Paragios, and R. Deriche, "Implicit active shape models for 3-D segmentation in MR imaging," *MICCAI*, vol. 1, pp. 209–216, 2004.
[56] D. Cremers, N. Sochen, and C. Schnoerr, "A multiphase dynamic labeling model for variational recognition-driven image segmentation," *International Journal of Computer Vision*, vol. 66, no. 1, pp. 67–81, 2006.
[57] M. Rousson and D. Cremers, "Efficient kernel density estimation of shape and intensity priors for level set segmentation," *MICCAI*, vol. 2, pp. 757–764, 2005.
[58] D. Cremers, "Dynamical statistical shape priors for level set based tracking," *IEEE Trans. Pattern Anal. Mach. Intell.*, vol. 28, no. 8, pp. 1262–1273, Aug. 2006.
[59] C. Xu and J. L. Prince, "Snakes, shapes, and gradient vector flow," *IEEE Trans. Image Process.*, vol. 7, no. 3, pp. 359–369, Mar. 1998.
[60] Y. Chen, H. D. Tagare, S. Thiruvenkadam, F. Huang, D. Wilson, K. S. Gopinath, R. W. Briggs, and E. A. Geiser, "Using prior shapes in geometric active contours in a variational framework," *Int. J. Comput. Vis.*, vol. 50, pp. 315–328, 2002.
[61] D. Cremers, T. Kohlberger, and C. Schnorr, "Shape statistics in kernel space for variational image segmentation," *Pattern Recognit.*, vol. 36, no. 9, pp. 1929–1943, 2003.
[62] A. Tsai, A. Yezzi, W. Wells, C. Tempany, D. Tucker, A. Fan, W. W. Grimson, and A. Willsky, "A shape-based approach to the segmentation of medical imagery using level sets," *IEEE Trans. Med. Imag.*, vol. 22, no. 2, pp. 137–154, Feb. 2003.
[63] T. F. Cootes, C. J. Taylor, and D. H. Cooper, "Active shape models—Their training and application," *Comput. Vis. Image Understand.*, vol. 61, pp. 38–59, 1995.
[64] P. P. Smyth, J. Taylor, and J. E. Adams, "Automatic measurement of vertebral shape using active shape models," in *Proc. Br. Mach. Vis. Conf.*, 1996, pp. 705–714.
[65] N. Duta and M. Sonka, "Segmentation and interpretation of MR brain images: An improved active shape model," *IEEE Trans. Med. Imag.*, vol. 17, no. 6, pp. 1049–1067, Dec. 1998.
[66] G. Behiels, D. Vandermeulen, F. Maes, P. Suetens, and P. Dewaele, "Active shape modelbased segmentation of digital x-ray images," in *Lecture Notes in Computer Science*. Berlin, Germany: Springer-Verlag, 1999, pp. 128–137.
[67] M. Rogers, J. Graham, and R. A. Malik, "Exploiting weak shape constraints to segment capillary images in microangiopathy," *MICCAI*, pp. 717–726, 2000.
[68] R. Beare, "A locally constrained watershed transform," *IEEE Trans. Pattern Anal. Mach. Intell.*, vol. 28, no. 7, pp. 1063–1074, Jul. 2006.
[69] M. Pardas and P. Salembier, "Time-recursive segmentation of image sequences," in *EUSIPCO94*, Edinburg, U.K., 1994, pp. 18–21.
[70] B. Marcotegui and F. Meyer, "Bottom up segmentation of image sequences for coding," *Ann. Telecommun.*, vol. 52, no. 7–8, pp. 397–407, 1997.
[71] V. Grau, A. U. J. Mewes, M. Alcaniz, R. Kikinis, and S. K. Warfield, "Improved watershed transform for medical image segmentation using prior information," *IEEE Trans. Med. Imag.*, vol. 23, no. 4, pp. 447–458, Apr. 2004.
[72] C. Vachier and F. Meyer, "The viscous watershed transform," *J. Math. Imag. Vis.*, vol. 22, no. 2–3, pp. 251–267, 2005.
[73] N. Passat, C. Ronse, J. Baruthio, J.-P. Armspach, and J. Foucher, "Watershed and multimodal data for vessel segmentation: Application to the superior sagittal sinus," *Image Vision Comput.*, vol. 25, no. 4, pp. 512–521, Apr. 2007.
[74] P. Maragos, PDEs for morphological scale-spaces and eikonal applications [Online]. Available: http://citeseer.comp.nus.edu.sg/725784.html
[75] P. Maragos and M. Butt, "Curve evolution, differential morphology, and distance transforms applied to multiscale and eikonal problems," *Fundamenta Informaticae*, vol. 41, no. 1–2, pp. 91–129, 2000.
[76] F. Meyer, "Topographic distance and watershed lines," *Signal Process.*, vol. 38, pp. 113–125, 1994.
[77] L. Najman and M. Schmitt, "Watershed of a continuous function," *Signal Process.*, vol. 38, pp. 99–112, 1994.
[78] L. Najman and M. Schmitt, "Geodesic saliency of watershed contours and hierarchical segmentation," *IEEE Trans. Pattern Anal. Mach. Intell.*, vol. 18, no. 12, pp. 1163–1173, Dec. 1996.
[79] J. K. J. Park, "Snakes on the watershed," *IEEE Trans. Pattern Anal. Mach. Intell.* vol. 23, no. 10, pp. 1201–1205, Oct. 2001.
[80] F. Meyer and P. Maragos, "Multiscale morphological segmentations based on watershed, flooding and eikonal PDE, scale space," in *Proceedings of the Second International Conference on Scale-Space Theories in Computer Vision* . New York: Springer, 1999, vol. 1682, pp. 351–362.
[81] F. Meyer, "Topographic distance and watershed lines," *Signal Process.*, vol. 38, no. 1, pp. 113–125, Jul. 1994.